Supporting Information

for

Nature of Terrace Edge States (TES) in Lower-Dimensional Halide Perovskite

Kai Wang,*[#1] Tao Wu,[#2] Congcong Wu,[#3] Rammohan Sriramdas,[1] Xu Huang,[4] Ke Wang,[1] Yuanyuan Jiang,[1] Hairui Liu,[1] Yongke Yan,[1] Dong Yang,[1] Tao Ye,[1] Chang Liu,[5] Xiaowen Hu,[6] Xiaofang Jiang,[6] Shashank Priya*[1]

[1] Materials Research Institute, The Pennsylvania State University, University Park, PA 16802, United States
[2] Department of Mechanical Engineering, University of South Carolina, Columbia, SC 29208, United States
[3] Hubei Collaborative Innovation Center for Advanced Organic Chemical Materials, Key Laboratory for the Green Preparation and Application of Functional Materials, Hubei Key Laboratory of Polymer Materials, School of Materials Science and Engineering, Hubei University, Wuhan 430062, China
[4] School of Materials Science and Engineering, Southwest University of Science and Technology, Mianyang, Sichuan 621010, PR China
[5] Ningbo Institute of Materials Technology and Engineering (NIMTE), Chinese Academy of Science (CAS), Ningbo, Zhejiang 315201, PR China
[6] South China Academy of Advanced Optoelectronics, South China Normal University, Guangzhou 510006, PR China

SI 1. Single-crystalline sample characterization

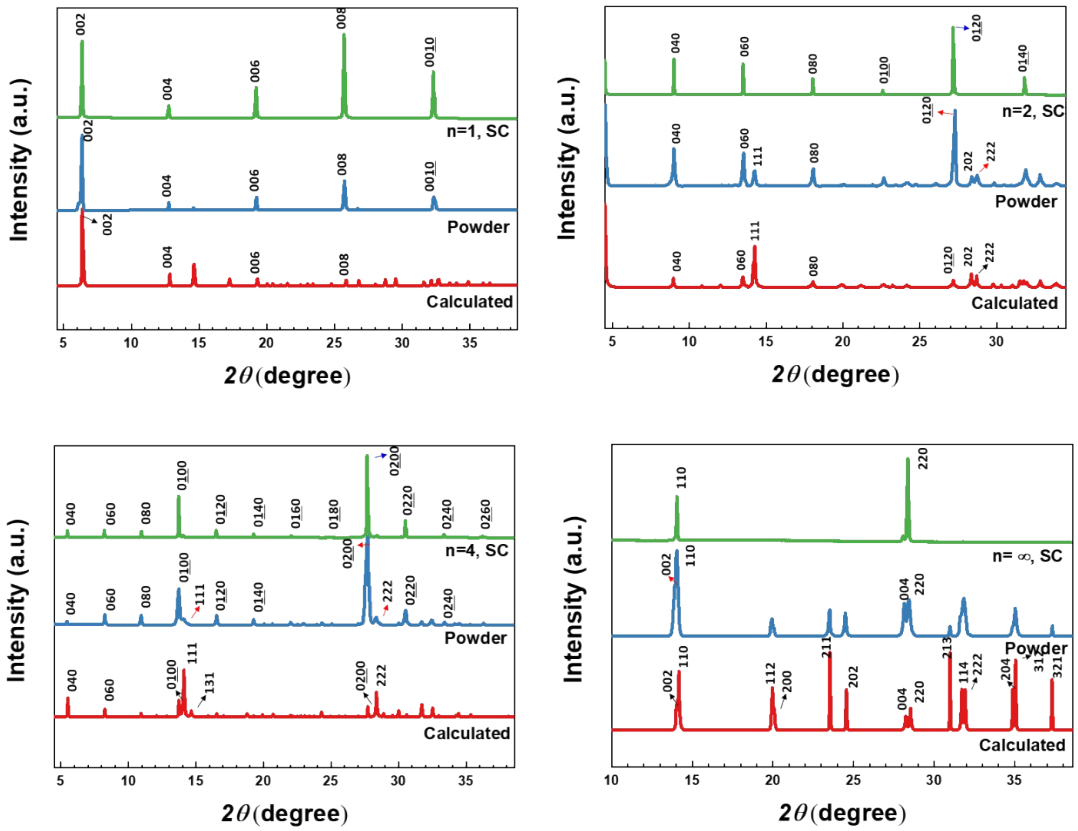

Figure S1. XRD of quasi-2D perovskite single-crystals (SCs), powder and calculated data.

The single-crystal flakes were synthesized according to reported methods.[1][2] The structure was confirmed by comparing the single-crystal and powder diffraction with the calculated values from reports. The consistency indicates the phase-purity and no foreign phases.

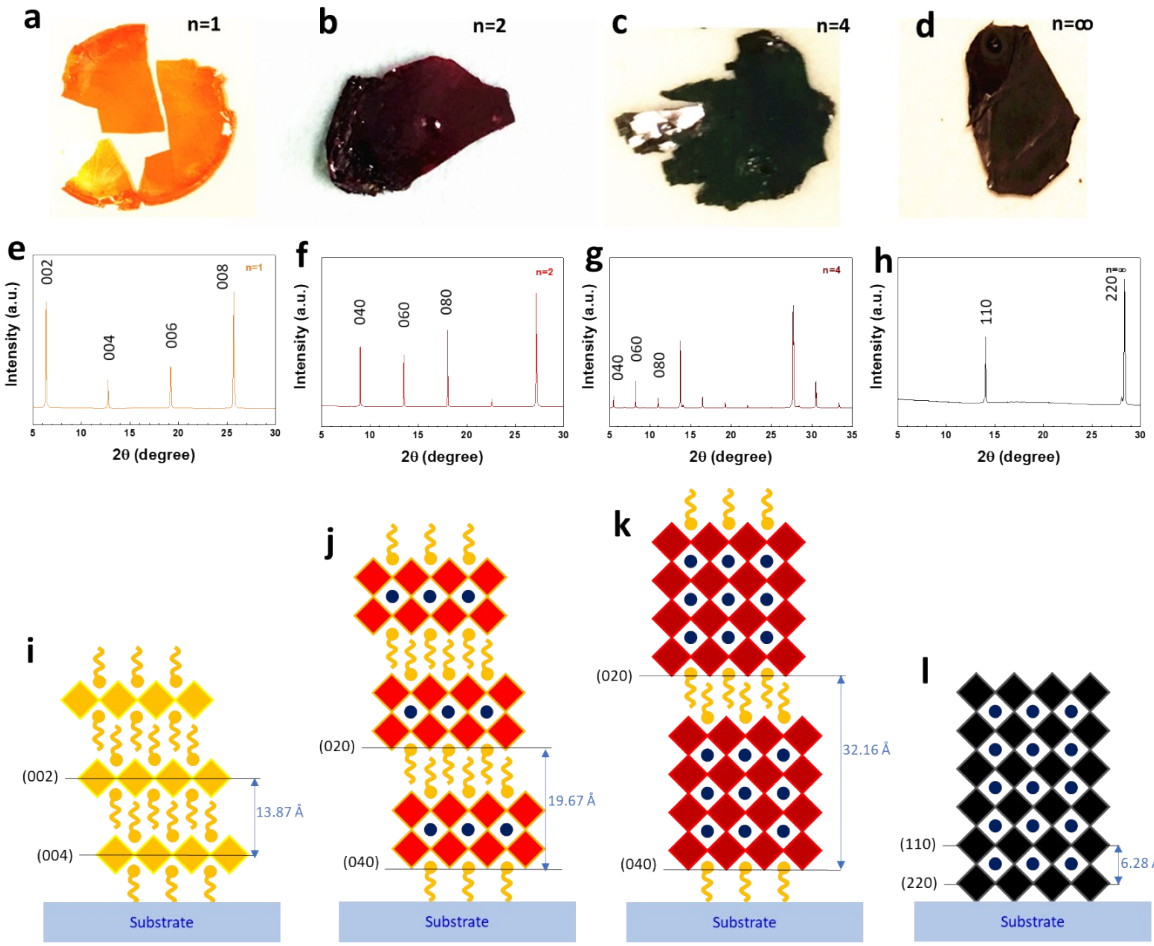

Figure S2. Halide perovskite single-crystalline flakes of $BA_2MA_{n-1}Pb_nI_{3n+1}$ (n=1, 2, 4 and ∞). (a-d) Photos of the single-crystalline flakes. (e-h) Corresponding XRD patterns and (i-l) schematics showing the flake samples are aligned in parallel with the substrate.

The single-crystalline flake samples of $BA_2MA_{n-1}Pb_nI_{3n+1}$ (n=1, 2, 4 and ∞) were synthesized from the water-air interface. **Figures S2a-d** display the photos of the flake samples. By laying the flakes on the substrates, we verified *via* XRD measurements that their out-of-lane directions are perpendicular to the substrates (**Figures S2e-l**).

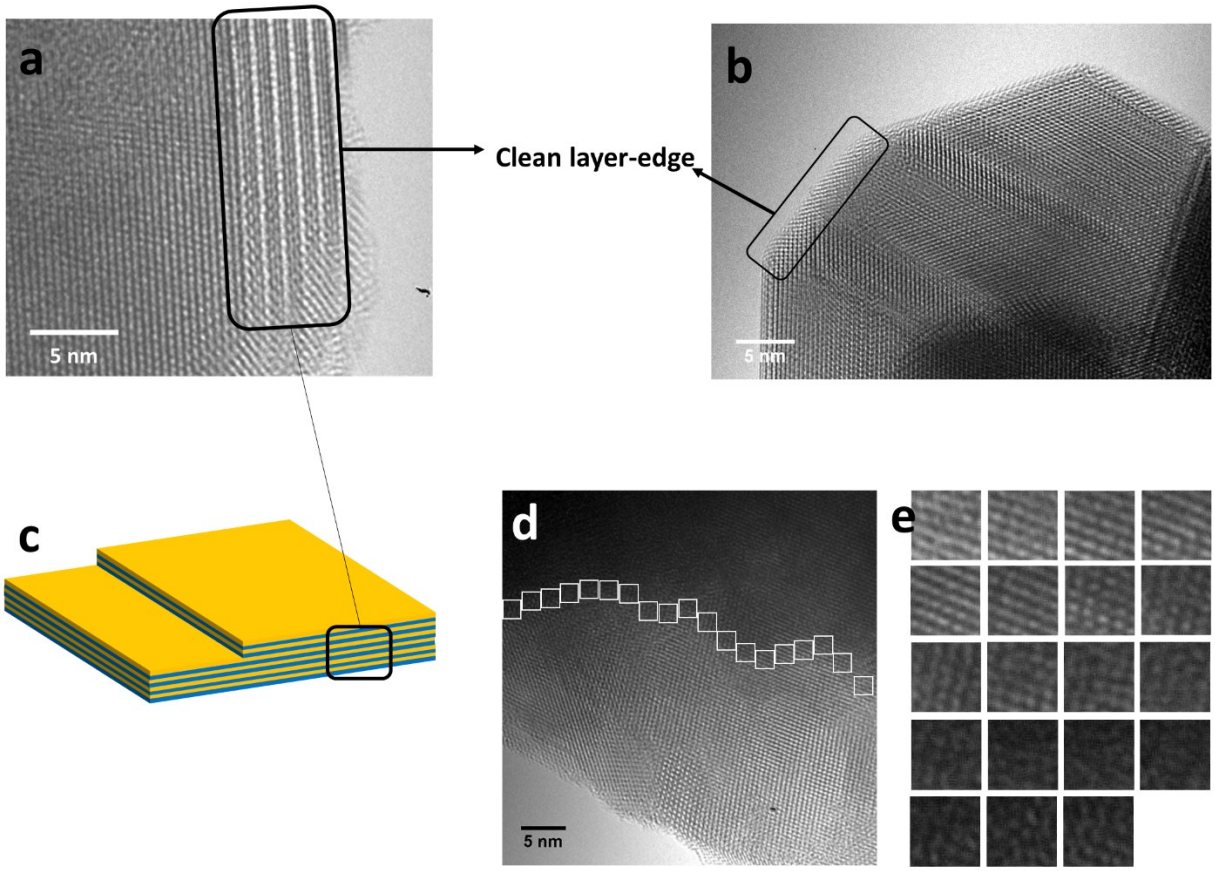

Figure S3. High-resolution transmission electron microscopy (HRTEM) of quasi-2D perovskite sample for identification of the layer-edge. (a) & (b) HRTEM images showing clean layer edges. The edge regions are denoted in the (c). (d) layer-edge region (denoted by 19 white squares in (e)) for extraction of the fast Fourier transform (FFT) at the layer-edge region.

SI 2. Calculation on the total collected charges at one terrace edge

The total collected charge during the tip scanning across one terrace edge can be calculated from the current profile, *i.e., I(x)*. Let the scan size be *L*, scan frequency be *f*, then the scan rate v is

$$v = 2Lf = \frac{dx}{dt} \qquad \text{(S1)}$$

Integration of the current profile with respect to *x*, we have

$$\int I(x)dx = \int \frac{dq}{dt}dx = \int v \cdot dq = v\int dq \qquad \text{(S2)}$$

Combining equations S1 and S2, the total collected charges at the terrace edge is

$$Q = \int dq = \frac{1}{2Lf}\int I(x)dx \qquad \text{(S3)}$$

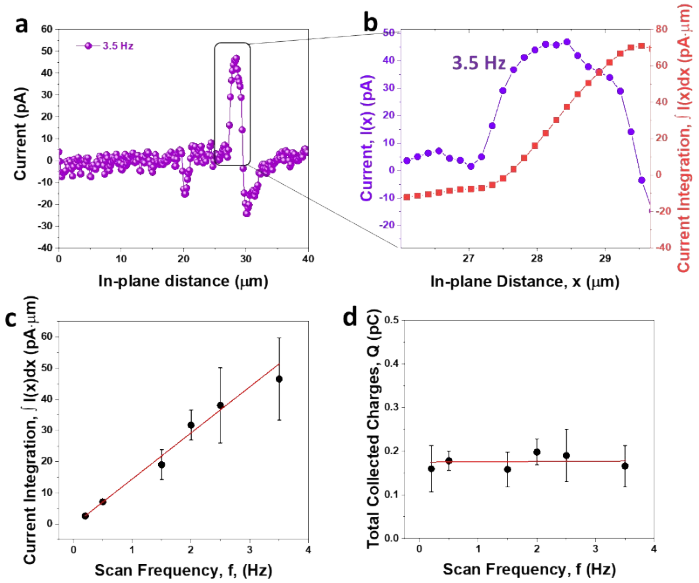

Figure S4. Total charge calculation. (a) Current profile at a scan rate of 3.5 Hz. (b) Magnified current profile at one terrace edge and corresponding current integration profile for charge calculation. (c) Current integration and (d) total collected charges calculated at from current integration profile at each scan frequency *vs.* scan frequency.

Figure S4a shows the current profile scanned at 3.5 Hz, the peak at x=28.3 μm was further magnified in **Figure S4b**. We plotted the current integration curve, $\int I(x)dx$, and obtained the total charge collected at this edge from equation S3, which is 164 fC. **Figure S4c** shows the current integration *vs.* scan frequency. **Figure S4d** displays the total collected charges calculated from the current integration curve at each frequency *vs.* the scan frequency. The results indicated the collected charges are independent with respect to the scan frequency. This can be understood by the fact that during the scanning across the edge, excited free charges are sufficiently extracted from the crystal edge states to the tip. The number of charge carriers during the extraction is fixed and not relevant to or the extraction is much faster than the time period during the scanning. Hence,

all the excited charges at the conductive edges are extracted. The average total charges are calculated to be 175 ± 32 fC.

SI 3. Edge height effects on the current intensity

The edge height difference is prepotential to the layer number of periodic stacking unit. In the case of $BA_2MA_3Pb_4I_{13}$ (n=4), as the minimal d-spacing is 32.16 Å, the edge height is then of 32.16m Å thick with m being 1, 2, 3, …. We further integrated the $I(x)$ with respect to x (**Figure S5a**) and calculated the total collected charges at the layer edges of different thicknesses. **Figure S5b** shows a linear dependence of total collected charges on the edge height, suggesting that the charge number density is a constant value belonging to the intrinsic property of the crystal layer edge states.

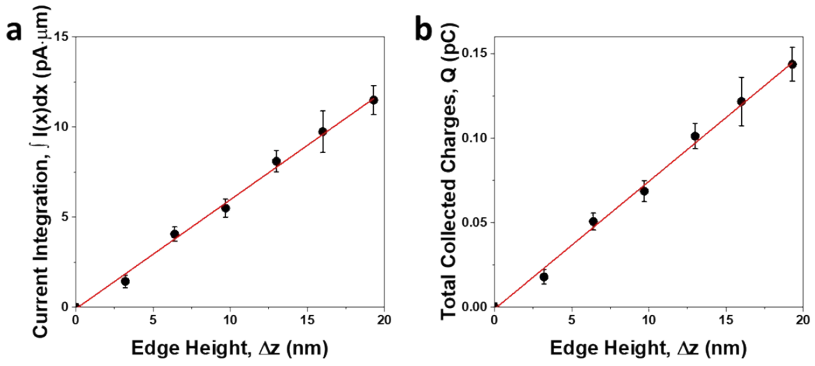

Figure S5. Edge height dependence of collected charges at the terrace edge. (a) Current integration and (b) total collected charges calculated at from current integration profile at different edge heights *vs.* edge height.

We also measured the peak current at layer-edges from different samples of $BA_2MA_{n-1}Pb_nI_{3n+1}$ (n=1, 2, 4 and ∞), the raw data was listed in **Table S1 (SI 4)**. The edge current is normalized to unit scan frequency as they are linearly dependent on the frequency. By plotting the edge current (normalized to unit scan frequency) vs. the edge height difference, Δz. We found for different materials, the linear dependence of current on Δz dominates. Even at higher edge height to 500 nm, the linear dependence applies as well.

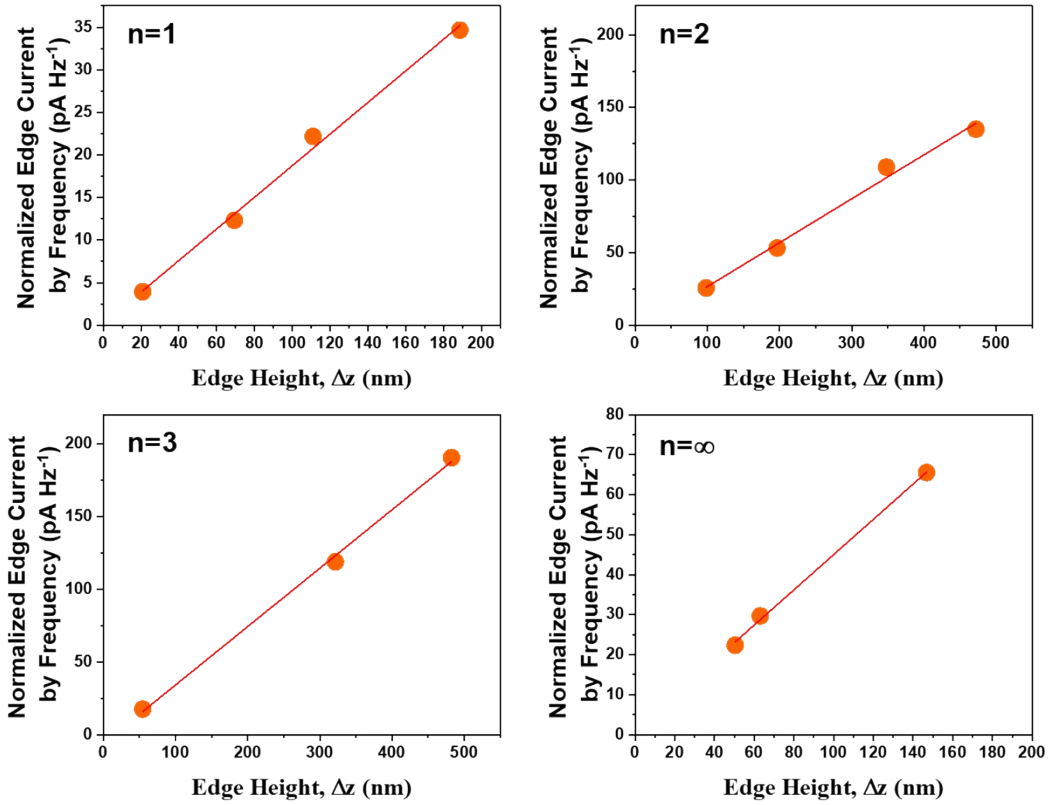

Figure S6. Normalized edge current with regarding to the edge height difference from various $BA_2MA_{n-1}Pb_nI_{3n+1}$ (n=1, 2, 4 and ∞) samples.

SI 4. Peak current *vs.* index *n*

The peak current at the layer-edges from different samples of $BA_2MA_{n-1}Pb_nI_{3n+1}$ (n=1, 2, 4 and ∞) is further compared. **Table S1** shows the current values, edge height difference, and scan frequency obtained from different experiments, along with the quantum structures of different samples. The loading force was controlled at the same value to minimize the interference of the contact area. As the current is linearly dependent on the scan frequency and edge height difference, we normalized the current to unit height and unit frequency. The normalized peak current is then plotted with regarding to the index n. As shown in **Figure S7a**, the normalized peak current increases along with the index n, but not showing a linear dependence. It should be noted that for $BA_2MA_{n-1}Pb_nI_{3n+1}$ (n=1, 2, 4 and ∞), index n denotes the layer number of [PbI_6] octahedra and correlates with the quantum well thickness. As can be seen in **Figure S7b**, in the $BA_2MA_3Pb_4I_{13}$

(n=4) multiple quantum well (MQW), there are four layers of [PbI_6] octahedra, corresponding to a quantum well (QW) thickness (l_{QW}) of 25.2 Å. The quantum barrier (QB) thickness (l_{QB}) is corresponding to the BA organic spacer. We then plot the curve of normalized current *vs.* $l_{QW}/(l_{QW}+l_{QB})$ in **Figure S3c**. It is found that the peak current across the layer edge is linearly dependent on the "well thickness concentration", *i.e.,* $l_{QW}/(l_{QW}+l_{QB})$, suggesting the contribution to the current mainly comes from the [PbI_6] octahedra QW rather than the BA organic spacer. On the other hand, in our Confocal fluorescence microscopy (CFM) measurement (in **Figure 5c-g** in the main text), we also found the red-shifted photoluminescence at the layer edge, suggesting the distinct layer edge states close to the band edge. For organic-inorganic quasi-2D halide perovskite, the band edge (conduction band bottom and valance band top) is mainly contributed by the Pb 6s & 6p and I 5s & 5p orbitals.[3] Hence, the layer edge states are most likely related with the inorganic [PbI_6] octahedra.

Table S1 Peak current values obtained from various samples of $BA_2MA_{n-1}Pb_nI_{3n+1}$ (n=1, 2, 4 and ∞), along with their edge height difference, scan frequency, crystal unit length (z-direction), quantum well (l_{QW}) and quantum barrier (l_{QB}) thickness, as well as the normalized current.

n	Unit length (nm)	l_{QW} (nm)	l_{QB} (nm)	current (pA)	height (nm)	frequency (Hz)	normalized current (pA/nm/Hz)
1	1.387	0.628	0.759	5.9	20.8	1.5	0.189
1	1.387	0.628	0.759	121.3	188.6	3.5	0.183
1	1.387	0.628	0.759	77.6	110.9	3.5	0.199
1	1.387	0.628	0.759	43.1	69.3	3.5	0.177
2	1.967	1.256	0.711	21.8	348.1	0.2	0.313
2	1.967	1.256	0.711	202.5	472.0	1.5	0.285
2	1.967	1.256	0.711	38.5	98.3	1.5	0.260
2	1.967	1.256	0.711	79.8	196.7	1.5	0.270
4	3.216	2.512	0.704	3.5	54.6	0.2	0.320
4	3.216	2.512	0.704	285.6	482.4	1.5	0.394
4	3.216	2.512	0.704	178.2	321.6	1.5	0.369
∞	0.628	0.628	0	13.1	146.7	0.2	0.446
∞	0.628	0.628	0	44.5	63.0	1.5	0.470
∞	0.628	0.628	0	33.5	50.4	1.5	0.443

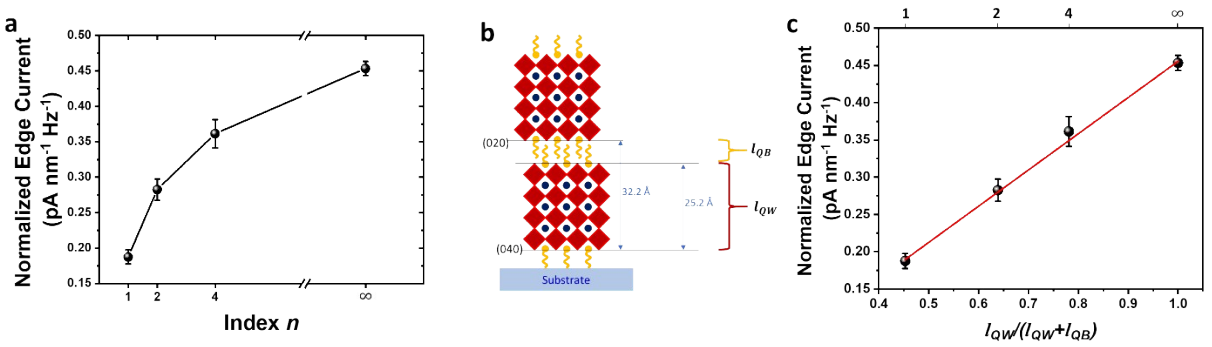

Figure S7 Layer edge current dependence on the quantum structure of $BA_2MA_{n-1}Pb_nI_{3n+1}$ (n=1, 2, 4 and ∞). (a) Normalized edge current *vs.* index n. (b) A schematic of multi-quantum well (MQW) structure of $BA_2MA_3Pb_4I_{13}$ (n=4), showing the quantum well thickness (l_{QW}) and quantum barrier thickness (l_{QB}). (c) Normalized edge current vs. $l_{QW}/(l_{QW}+l_{QB})$.

SI 5 Nanocontact between tip and sample

Hertz model was utilized to determine the contact geometry at the tip/sample interface. The load force, L, can be expressed by the simplified equation of

$$L = 4/3\frac{E}{1-\nu^2}\sqrt{r_t}\delta^{3/2} \qquad \text{(S4)}$$

where E is the Young's modulus and ν is the Poisson's ratio of the sample, r_t is the radius of tip curvature (20 nm), δ is the indentation depth.[4] As in the load force analysis (**Figure 3g-i**), the sample of $BA_2MA_3Pb_4I_{13}$ (n=4) was employed, the out-of-plane $E = 7$ GPa and $\nu = 0.3$ was then assigned according to previous reports. We further calculated the δ under each load force, as shown in the **Table S2**.

Table S2 Geometric feature of the tip-sample contact at different load forces.

L, nN	ν	E, GPa	r_t, nm	δ, nm	A, nm^2
1.6	0.3	7	20	0.11	13.4

6.0	0.3	7	20	0.26	32.2
15.0	0.3	7	20	0.47	58.9

The contact geometry is then schematized in **Figure S8a**. We also employed the finite element method (FEM) simulation to estimate the 'effective area', A_{eff}. The FEM simulation of the electric field distribution at the probe-sample interface was performed by utilizing the 2D electrostatic module from the COMSOL Multiphysics software. The dielectric constant, ε_r of the 2D halide perovskite MQW was calculated from the equation of

$$\varepsilon_r = \sqrt{\varepsilon_w \varepsilon_b \frac{\varepsilon_w l_w + \varepsilon_b l_b}{\varepsilon_b l_w + \varepsilon_w l_b}} \qquad \text{(S5)}$$

where $\varepsilon_w = 6.1$, $\varepsilon_b = 2.4$ are the dielectric constant of QW and barrier layer, $l_w = 24.6$ Å and $l_b = 7.6$ Å are the thickness of the QW and barrier layer.[5] For $BA_2MA_3Pb_4I_{13}$ (n=4), ε_r is calculated to be 4.8. **Figure S8b** shows the simulated electric field distribution at the tip-sample interface. We found the electric field, E, intensifies at the contact fringe and decays significantly in penetrating the inner sample. As shown in **Figure S8c**, at *ca.* $r_{eff} = 2.9r$, with r being the radius of the real contact area, the E decays by one order of magnitude, which is in good agreement with the prediction from the previous numerical method ($d \simeq 3r$).[6] Then we estimated the A_{eff} =8.4A. By normalizing I with estimated A, the current density, J, can be calculated. The current density is then plotted in **Figure S8d** with respect to load force, showing a constant current density.

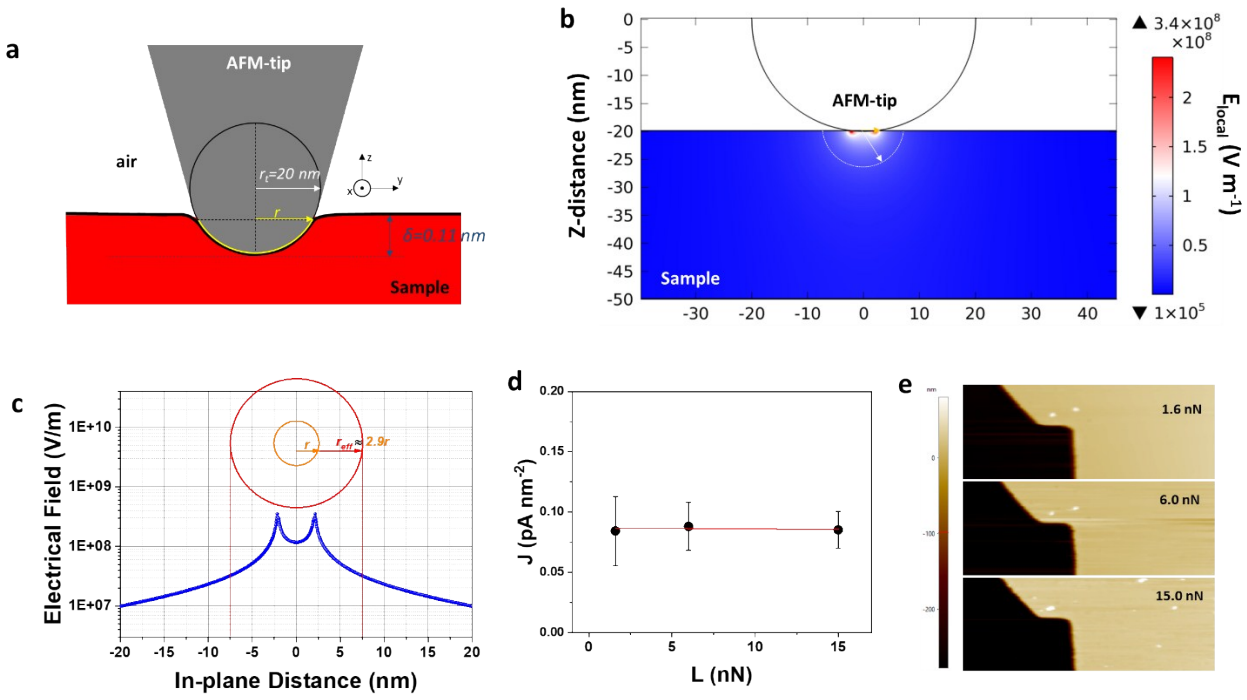

Figure S8. Nanocontact between tip and sample. (a) The contact geometry, where r_t is the tip radius, *r* is contact radius, δ is the indentation. (b) Simulated electric field distribution at the tip-sample interface. (c) Line analysis of the local electrical field, E versus the distance to the axis of symmetry simulated by FEM. The E intensifies at the fringe of the tip/sample contact and decays by one order of magnitude at the distance of ca. 2.9r. Hence, it can be considered that the radius of the effective electrical contact area, A_{eff}. (d) Current density *vs.* the load force. (e) Topography images corresponding to the CGM in **Figure 3G**, showing no topographical change upon different loads.

SI 6 Current direction upon tip-sample dynamics

The current sign reversion is also observed in other samples. As shown in **Figure S9**, tracing and retracing scans gave different polarity of the current.

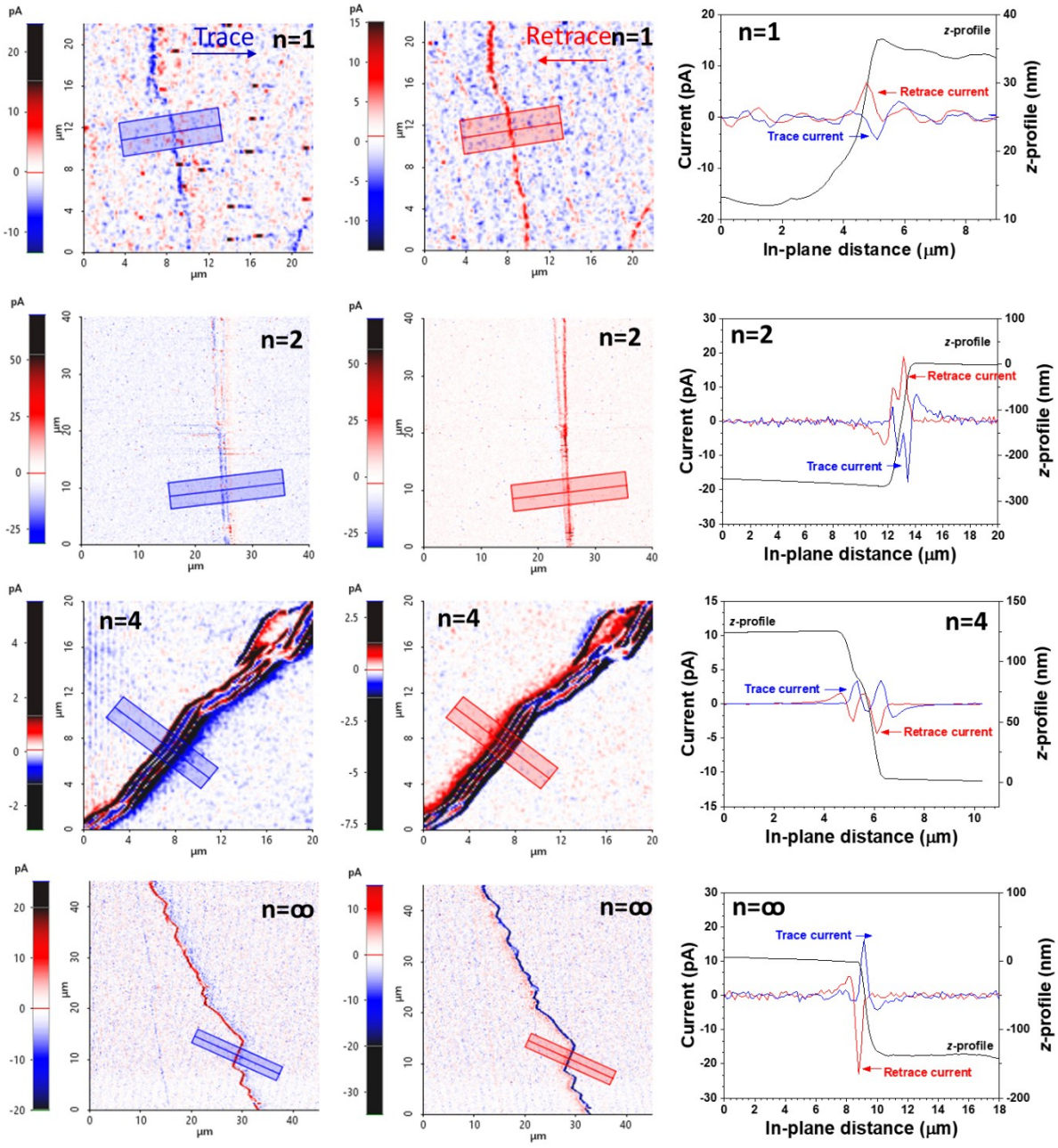

Figure S9. Scan direction effect on the current sign. Tracing, retracing and corresponding current- and z-profiles of different perovskite samples.

Focusing on the tip-sample relative movement, every time the tip moves uphill the sample edge, the current shows a negative current, indicating the electrons are extracted from sample to tip (or can be regarded as hole injection from tip to sample); oppositely, whenever the tip moves downhill

the sample edge, the current exhibits a positive current, suggesting the electrons are injected from the tip to the sample. This can be understood by taking consideration of the competitive relationship between electron consumption and refilling at the terrace edges. **Figure S10** schematizes the possible mechanism. In **Figure S10a**, the CGM tip climbs uphill the terrace edge. The CGM conductive tip has been reported to able to scrap the screen charges at the domain walls in ferroelectric materials.[7][8] In this study, during the ascending moving of the conductive CGM tip, scraping of terrace edge electrons by the tip front lowered down the electrical potential there, which induced the hole injection from the tip to the sample (**Figure S10a, (ii)**). The terrace electron replenishment at the trailing edge of the tip can be achieved by refilling from the ambient or from the inner sample (**Figure S10a, (iv)**).[9] Thus, during the tip ascending the terrace edge, the current flow is motivated by the consumption from the recombination of scarped electrons with injected holes or the electron extraction from sample to probe. On the other hand, in the case of tip descending (**Figure S10b**), during the tip moving downhill the terrace edge, the edge electrons are being razed away by the tip front due to the mechanical impact transferred to them and possibly the repulsive force from neighboring charges (**Figure S10b, (ii)**).[9] In this situation, the edge electrons are being supplied by the electron injection from the grounded tip and being deposited on the edge surface (**Figure S10b, (iii)**). As such, a current flowing from the sample to the tip motivated by the refilling, is formed, representing a positive current detection.

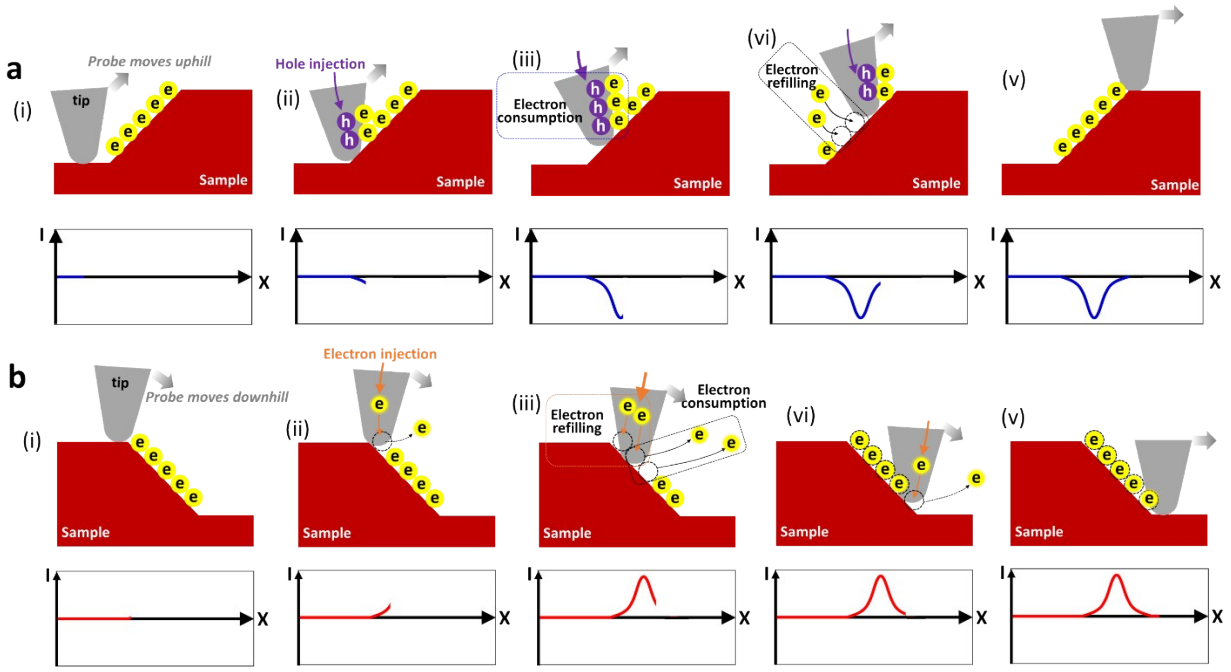

Figure S10. The possible mechanism for the current sign conversion at terrace edge. (a) Tip ascending and (b) tip descending the edge.

SI 7 Difference between quasi-2D perovskite and ferroelectric materials

Previous reports on CGM technique investigated the periodically poled lithium niobate (PPLN) single crystal sample. Artificial domain walls were created by applying electrical bias and the CGM technique was then employed to distinguish the conductive domain walls. However, for the halide perovskites, there is a wide argument on the existence of their ferroelectricity. No solid evidence supporting the ferroelectricity of $BA_2MA_{n-1}Pb_nI_{3n+1}$ (n=1, 2, 4 and ∞) perovskites has been reported. We hence carried out the piezoresponse force microscopy (PFM) and polarization-electric field measurements to determine their ferroelectricity from both microscopical and macroscopical views. **Figure S11** shows the corresponding images of PFM measurement. We chose a 10×10 μm region with a prevalent layer edge step (**Figure S11 a&d**). Neither piezoresponse phase nor amplitude images show typical "ferroelectric domain" feature (**Figure S11b,c,e,f**) as ferroelectric materials (*e.g.*, $PbZr_{0.44}Ti_{0.56}O_3$ (PZT)) do (**Figure S11 g&h**).

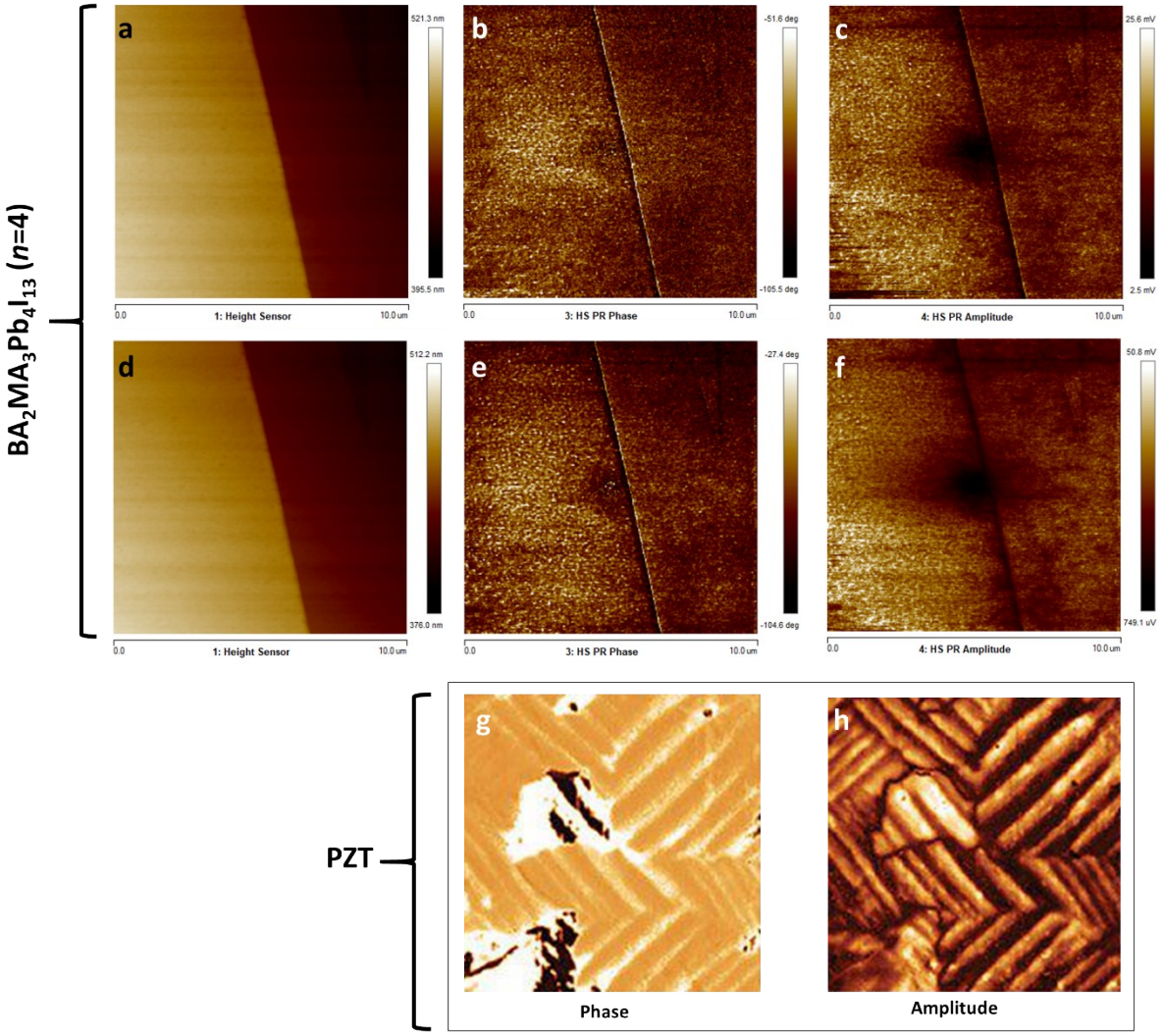

Figure S11. PFM measurements on $BA_2MA_3Pb_4I_{13}$ (n=4) sample and typical images of a $PbZr_{0.44}Ti_{0.56}O_3$ (PZT) ferroelectric material. (a) Surface morphology, (b) piezoresponse phase and (c) amplitude images of $BA_2MA_3Pb_4I_{13}$ (n=4) sample at the 1 V condition. (d) Surface morphology, (e) piezoresponse phase and (f) amplitude images of $BA_2MA_3Pb_4I_{13}$ (n=4) sample at the 2 V condition. Typical (g) phase and (h) amplitude images of a ferroelectric material (PZT), showing ferroelectric domains clearly, adapted from https://afm.oxinst.com/gallery/piezoresponse-force-microscopy-afm-image-gallery.

We also investigated the I-V curve of a bulk sample of $BA_2MA_3Pb_4I_{13}$ (n=4). As shown in **Figure S12a**, the I-V curve exhibits a good match between the forward and reverse scan and no obvious hysteresis was obtained. It should be noted that typical ferroelectric materials display a dramatic increase in current at a coercive field (as can be seen in **Figure S12e**). Such different I-V behavior between $BA_2MA_3Pb_4I_{13}$ (n=4) and ferroelectrics implies a distinction of

ferroelectricity between them. Although some other non-symmetric perovskite materials have been reported,[10][11] no direct evidence has been released to classify the $BA_2MA_3Pb_4I_{13}$ into the ferroelectric materials. Even for the prototype $MAPbI_3$, there are reports disclose the absence of ferroelectricity.[12] To further clarify the absence or presence of ferroelectricity in $BA_2MA_3Pb_4I_{13}$, we then study the dielectric constant dependence on the applied electric field (**Figure S12 b&c**). Typical polarization-electric field (P-E) loop can be obtained from the dielectric constant according to the equation of[13]

$$\Delta P = \varepsilon_0 \int \varepsilon \cdot \partial E \qquad \text{(S6)}$$

where ΔP is the change in polarization, and ε_0 is the vacuum permittivity. It should be noted classic, insulating ferroelectric materials usually exhibit a distinctive dependence of dielectric constant on an applied electric field. For such ferroelectric materials, the real part of the dielectric constant, ε_{re}, dominates the complex dielectric constant. The imaginary part, ε_{im} is commonly neglected. In some ferroelectric materials with high defect concentrations, however, leakage currents, which are relative to ε_{im}, generally increase dramatically and become a significant part of the response. In the case of $BA_2MA_3Pb_4I_{13}$ (**Figure S12 b&c**), neither ε_{re} nor ε_{im} exhibit any hysteresis loop with regarding to the electric field. We calculated the polarization on basis of ε_{re} and ε_{im}, respectively. Neither of them displays an obvious P-E hysteresis (yellow line in **Figure S12 b&c**). This is significantly different from typical ferroelectric materials (a clear P-E loop can be seen, **Figure S12 d&e**).

Hence, as neither ferroelectric domains nor macroscopical ferroelectric hysteresis was observed in the $BA_2MA_3Pb_4I_{13}$, the conductive layer edge in this study is different from the ferroelectric domain wall reported in PPLN.

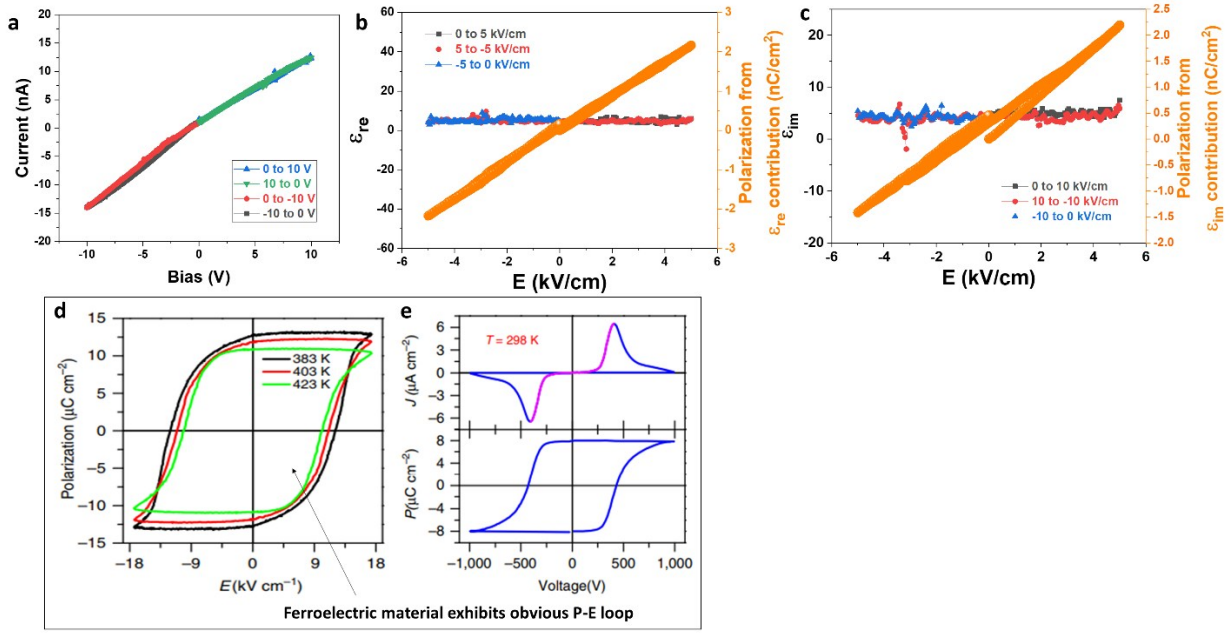

Figure S12. Ferroelectricity study of $BA_2MA_3Pb_4I_{13}$ (*n*=4). (a) I-V curve of a bulk sample. (b) Real and (c) imaginary part of the dielectric constant *vs.* electric field, coupled with the calculated polarization vs. electric field (P-E loop). (d) Typical P-E loop of a ferroelectric material. (e) I-V and P-V loop of a ferroelectric material. (d) & (e) are adapted from reference[14].

SI 8 Fermi level determination from Kelvin probe force microscopy (KPFM) measurement

KPFM measurement acquires the contact potential difference (CPD) signal between the sample surface and tip. To determine the work function of the sample surface, we need to know the work function of the tip. We employed the standard reference to firstly calibrate the tip work function and then use it to determine the Fermi level of the sample at different its topographical regions. **Figure S13** shows the KPFM measurement of a standard HOPG reference (fresh cleavage before measurement) that has a work function of 4.6 eV. Hence, the Fermi level of the $BA_2MA_3Pb_4I_{13}$ (*n*=4) sample can be determined from the CPD images.

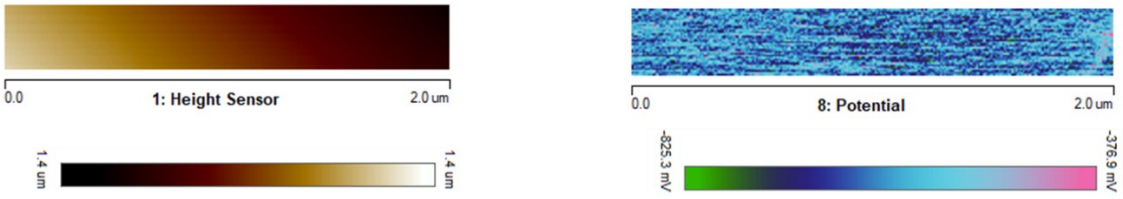

Figure S13. KPFM measurement on a highly oriented pyrolytic graphite (HOPG) reference for determination of the tip work function.

SI 9 Repeat CGM scan

The ion migration is on the basis that mobile ions play the role of charge carriers, which will lead to mass transport and change the final topography after several scanning times. Shao et al found the ion movement by poling can significantly change the morphology of the perovskite thin film.[15] We then checked the scanning repeatability of the CGM measurement on the quasi-2D samples. **Figure S14** shows the CGM images of the same region under different scanning times from 2 to 24 cycles. The current profile was further extracted to check the repeatability. It is found that the edge exhibits a constant current value regardless of the scanning times (**Figure S14c**).

We also compared the surface morphology during the scanning history (**Figure S15a**). The very first scanned image is identical to the last image with 24 times repeat. The topographies with or without multiple scanning match very well, as can be seen from the z-profile coincidence in **Figure S15c**. Hence, there is no obvious change in the surface morphology, which is different from the clear observation of ion migration in perovskite thin film.[15]

Based on above analysis as well as the clean crystal edge without impurities or vacancies (observed in HRTEM, Figure S3a &b), we conclude the edge current detected in the CGM measurement is not due to the ion conduction that may typically be present in perovskite thin films (in thin films, amorphous phase and mobile ions may exist).

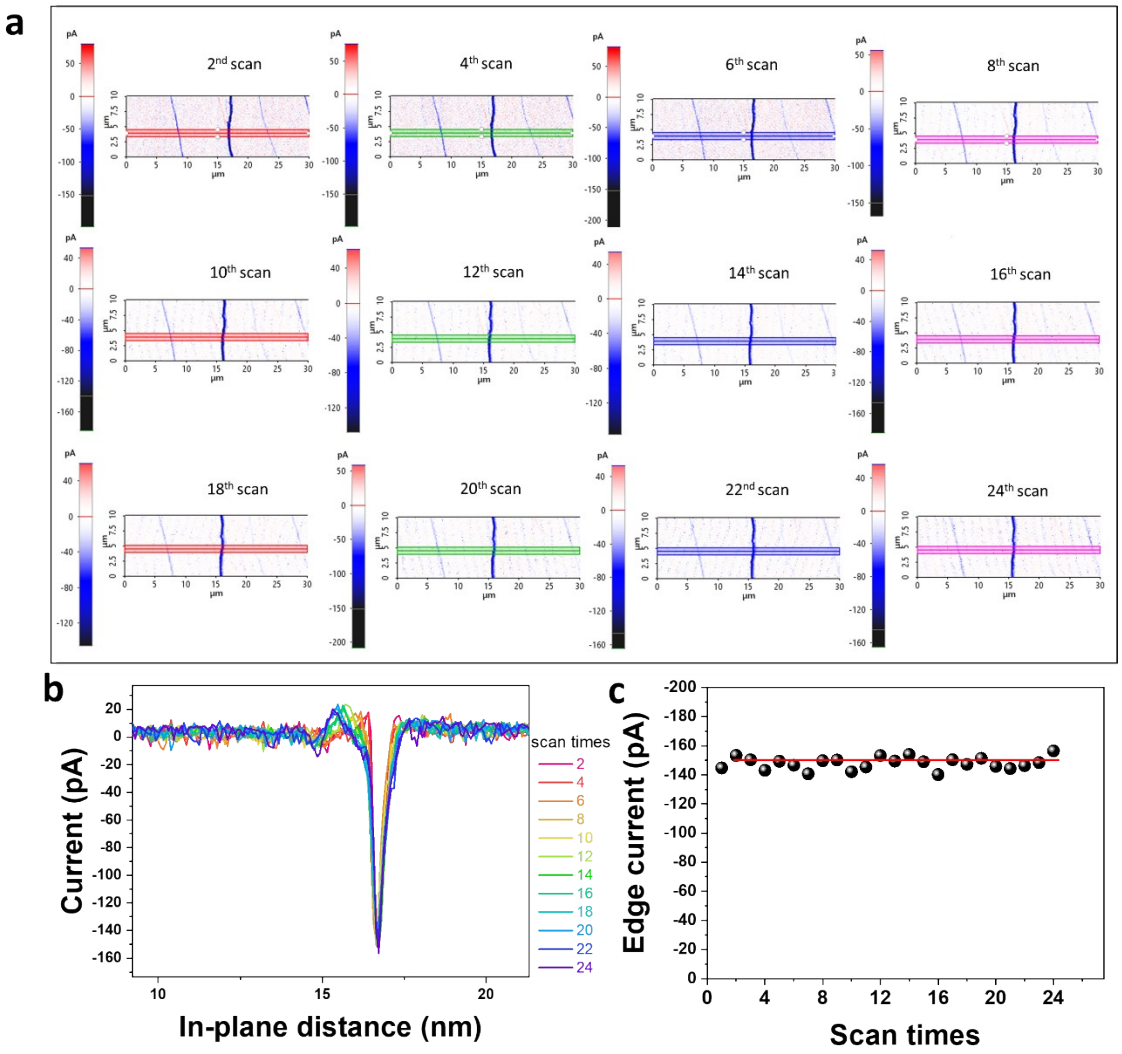

Figure S14. Repeat CGM scans for 24 times at the same region. (a) CGM images after repeat scanning at different times. (b) Current profile at the local region across the layer edge. (c) The peak current at the edge (located at the in-plane distance of ca. 15 μm) in relation with the repeating times.

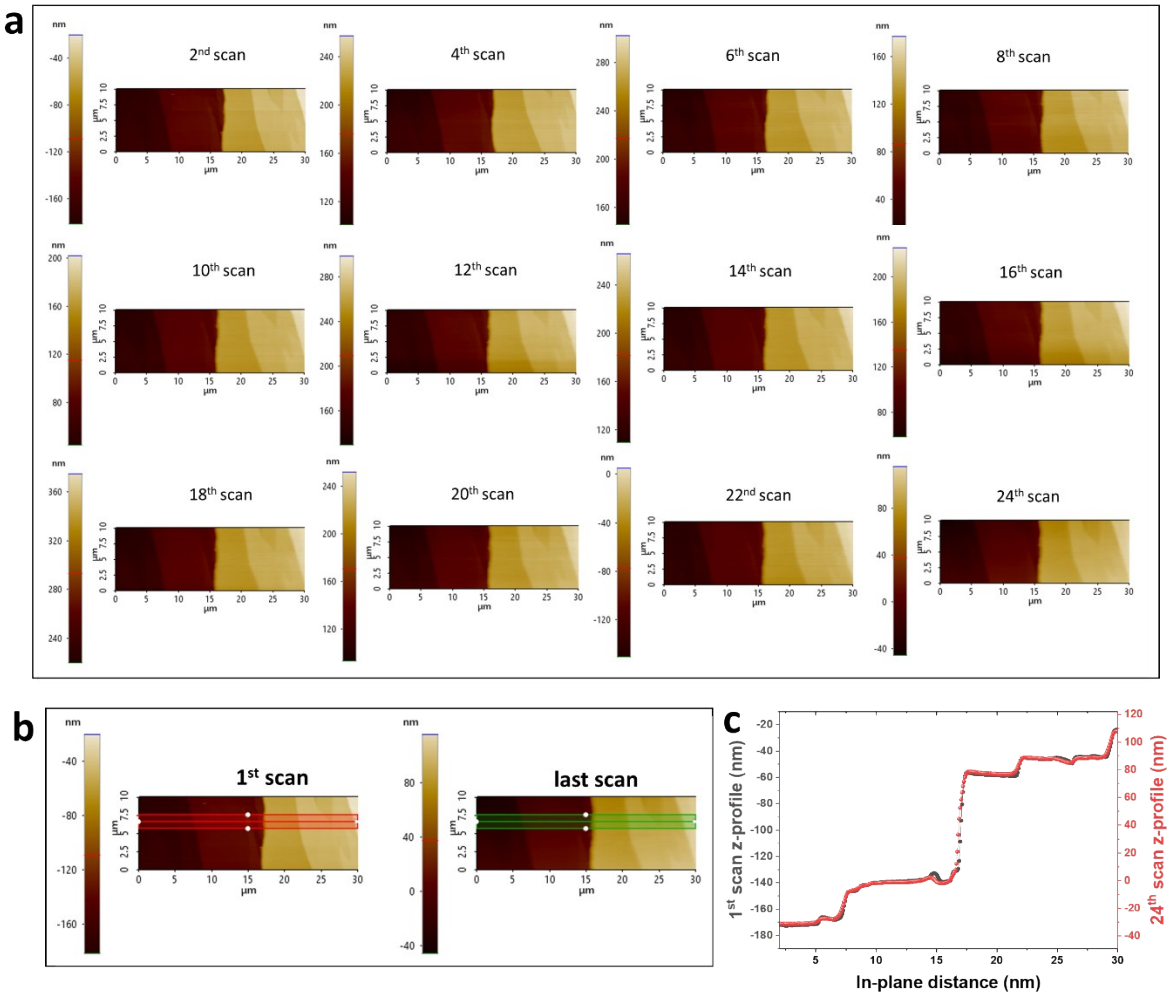

Figure S15. Repeat scans for 24 times at the same region. (a) Topography images after repeat scanning at different times. (b) Comparison of the first and last topography image of the region. (c) Comparison of the z-profile along the selected regions in (b).

SI 10 First-principles density function theory (DFT) calculations

Fig. S16a shows the projected density of states (DOS) of bulk-BA_2PbI_4 and **Fig. S16b** displays the projected density of states (DOS) profiles for surface-BA_2PbI_4.

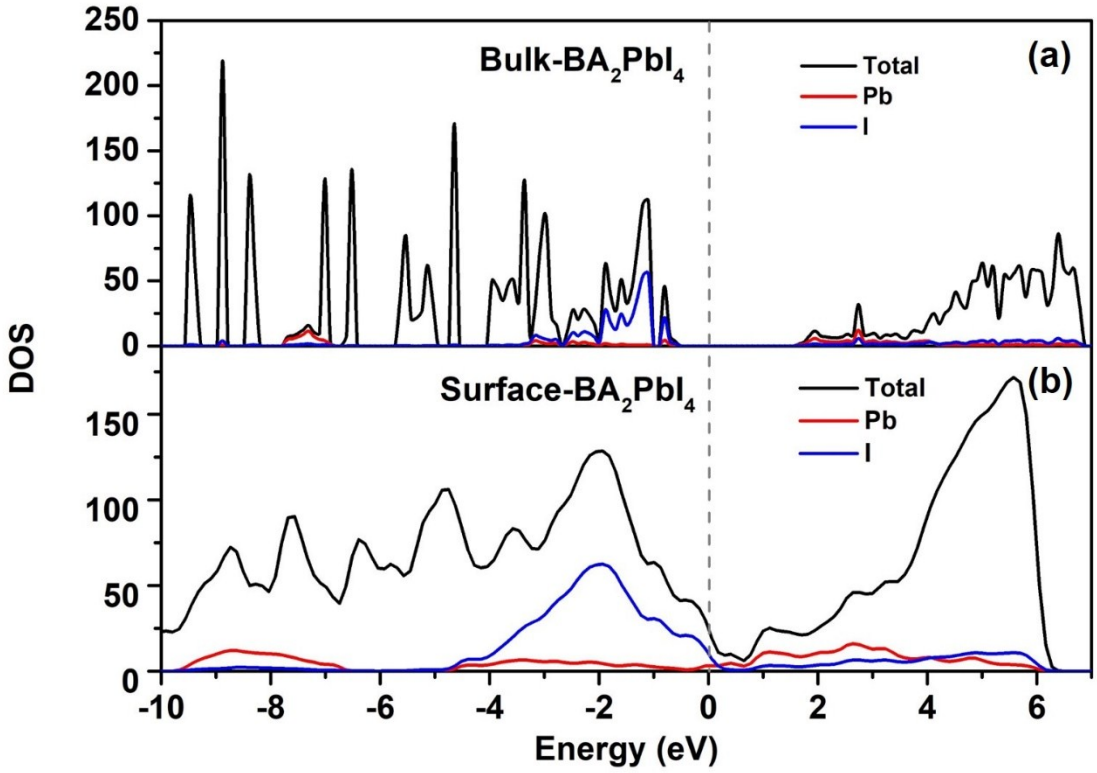

Figure S16. (a) The projected density of states (DOS) profiles for bulk-BA_2PbI_4, (b) The projected density of states (DOS) profiles for surface-BA_2PbI_4.

Reference

[1] K. Wang, C. Wu, D. Yang, Y. Jiang, S. Priya, *ACS Nano* **2018**, *12*, 4919.

[2] K. Wang, D. Yang, C. Wu, J. Shapter, S. Priya, *Joule* **2019**, *3*, 311.

[3] S. Silver, J. Yin, H. Li, J.-L. Brédas, A. Kahn, *Adv. Energy Mater.* **2018**, *8*, 1703468.

[4] Q. Tu, I. Spanopoulos, S. Hao, C. Wolverton, M.G. Kanatzidis, G.S. Shekhawat, V.P. Dravid, *ACS Appl. Mater. Interfaces* **2018**, *10*, 22167.

[5] X. Hong, T. Ishihara, A. V. Nurmikko, *Phys. Rev. B* **1992**, *45*, 6961.

[6] M. Alexe, D. Hesse, *Nat. Commun.* **2011**, *2*, 256.

[7] S. Tong, I.W. Jung, Y.-Y. Choi, S. Hong, A. Roelofs, *ACS Nano* **2016**, *10*, 2568.

[8] Y.-Y. Choi, S. Tong, S. Ducharme, A. Roelofs, S. Hong, *Sci. Rep.* **2016**, *6*, 25087.

[9] S. Hong, S. Tong, W.I. Park, Y. Hiranaga, Y. Cho, A. Roelofs, *Proc. Natl. Acad. Sci. U. S. A.* **2014**, *111*, 6566.

[10] H.-Y. Ye, Y.-Y. Tang, P.-F. Li, W.-Q. Liao, J.-X. Gao, X.-N. Hua, H. Cai, P.-P. Shi, Y.-M.

You, R.-G. Xiong, *Science* **2018**, *361*, 151.

[11] W.-Q. Liao, Y. Zhang, C.-L. Hu, J.-G. Mao, H.-Y. Ye, P.-F. Li, S.D. Huang, R.-G. Xiong, *Nat. Commun.* **2015**, *6*, 7338.

[12] M. Sajedi Alvar, M. Kumar, P.W.M. Blom, G.-J.A.H. Wetzelaer, K. Asadi, *AIP Adv.* **2017**, *7*, 095110.

[13] Y. Rakita, O. Bar-Elli, E. Meirzadeh, H. Kaslasi, Y. Peleg, G. Hodes, I. Lubomirsky, D. Oron, D. Ehre, D. Cahen, *Proc. Natl. Acad. Sci.* **2017**, *114*, E5504.

[14] W.-Q. Liao, Y. Zhang, C.-L. Hu, J.-G. Mao, H.-Y. Ye, P.-F. Li, S.D. Huang, R.-G. Xiong, *Nat. Commun.* **2015**, *6*, 7338.

[15] Y. Shao, Y. Fang, T. Li, Q. Wang, Q. Dong, Y. Deng, Y. Yuan, H. Wei, M. Wang, A. Gruverman, J. Shield, J. Huang, *Energy Environ. Sci.* **2016**, *9*, 1752.